A Novel Combined Experimental and Multiscale Theoretical Approach to Unravel the Structure of SiC/SiO$_x$ Core/shell Nanowires For Their Optimal Design †

Tommaso Morresi,*[ab] Melanie Timpel,*[cd] Andrea Pedrielli,[ab] Giovanni Garberoglio,[a] Roberta Tatti,[d] Roberto Verucchi,[d] Luca Pasquali,[efg] Nicola Maria Pugno,[b,h,i] Marco Vittorio Nardi*[cd] and Simone Taioli*[a,l]

In this work we propose a realistic model of nanometer-thick SiC/SiO$_x$ core/shell nanowires (NWs) using a combined first-principles and experimental approach. SiC/SiO$_x$ core/shell NWs were first synthesised by a low-cost carbothermal method and their chemical-physical experimental analysis was accomplished by recording X-ray absorption near-edge spectra. In particular, the K-edge absorption lineshapes of C, O, and Si are used to validate our computational model of the SiC/SiO$_x$ core/shell NW architectures, obtained by a multiscale approach, including molecular dynamics, tight-binding and density functional simulations. Moreover, we present ab-initio calculations of the electronic structure of hydrogenated SiC and SiC/SiO$_x$ core/shell NWs, studying the modification induced by several different substitutional defects and impurities into both the surface and the interfacial region between the SiC core and the SiO$_x$ shell. We find that on the one hand the electron quantum confinement results in a broadening of the band gap, while hydroxyl surface terminations decrease it. This computational investigation shows that our model of SiC/SiO$_x$ core/shell NWs is capable to deliver an accurate interpretation of the recorded X-ray absorption near-edge spectra and proves to be a valuable tool towards the optimal design and application of these nanosystems in actual devices.

1 Introduction

In recent decades, the discovery and synthesis of novel silicon (Si) nanostructures, such as Si dots and nanowires (NWs), have contributed to the rapid advancement of nano-science and nano-technology[1] to produce e.g. small transistors,[2] light emitting devices[3] or spin qubits for quantum computers.[4] Moreover, featuring one-dimensional (1D) geometry and high aspect ratio at the nanoscale,[5] Si nanostructures brought about fundamental interest in the scientific community to study the effect of reduced dimensionality onto the excitons and the electron-electron interaction.[6,7] In particular, Si NWs were found capable to achieve outstanding performances in catalysis,[8] energy harvesting[9,10] and storage,[11,12] chemical and biological sensing,[13,14] as well as application in bio–medicine.[15]

However, while a wide range of remarkable characteristics, most notably abundancy and the possibility of doping-induced modification of the electrical properties, makes Si by far the most widely used material for making electronics and optoelectronic devices, silicon carbide (SiC) offers wider band gap, larger critical electric fields and breakdown voltage, higher thermal conductivity and maximum operating temperature. These features make it probably the most promising alternative to replace Si in electronics devices working at high power/frequency or under prohibitive conditions.[16] Despite these peculiar properties, the use of SiC in electronics is not widespread. Major reasons for this are the high cost of production[17–19] and the high density of defects at the in-

[a] *European Centre for Theoretical Studies in Nuclear Physics and Related Areas (ECT*-FBK) and Trento Institute for Fundamental Physics and Applications (TIFPA-INFN), Trento, Italy, email: morresi@ectstar.eu; taioli@ectstar.eu*

[b] *Laboratory of Bio-Inspired and Graphene Nanomechanics, Department of Civil, Environmental and Mechanical Engineering, University of Trento, Italy*

[c] *Department of Industrial Engineering, University of Trento, Italy, email: melanie.timpel@unit.it; marcovittorio.nardi@unitn.it*

[d] *IMEM - CNR, Institute of Materials for Electronics and Magnetism, Trento unit, Trento, Italy*

[e] *IOM-CNR Institute, Trieste, Italy*

[f] *Engineering Department, University of Modena e Reggio Emilia, Italy*

[g] *Department of Physics, University of Johannesburg, South Africa*

[h] *Ket-Lab, Edoardo Amaldi Foundation, Italian Space Agency, Rome, Italy*

[i] *School of Engineering and Materials Science, Queen Mary University of London, United Kingdom*

[l] *Faculty of Mathematics and Physics, Charles University, Prague, Czech Republic*

† Electronic Supplementary Information (ESI) available: further details on ab initio simulations and experiments. See DOI: xxxxxxxxx

terface with the oxides in microelectronics applications. [20,21]

In particular, the synthesis of 1D SiC structures has attracted great interest due to the possibility of combining the material unique physical/chemical characteristics with low dimensionality. [22–24] The carbide mechanical properties are enhanced in NWs, showing super-plasticity at low temperature [25] and higher strength so that they can be used for toughening composites materials. [26] Furthermore, SiC nanowires show efficient electromagnetic wave absorption, [27,28] and their electronic properties have been exploited to realize field effect transistors [29] and efficient field emission sources. [30]

One common feature of Si-based NWs, regardless of the growth technique, is the presence of an amorphous silicon oxide (SiO_x) external layer coating the nanostructure. [24] By tuning the oxide layer thickness with respect to the SiC NW diameter in a core/shell architecture [31–33] one can modify both the electron emission [34,35] and the optical [32,36,37] properties of these systems. In addition, the SiO_x layer offers facile strategies to anchor organic molecules on the NWs' surface by chemical methods, paving the way for applications of functionalized SiC/SiO_x core/shell NWs in several fields, such as protective coatings, [38] biosensing [39] or as hybrid nanosystems for biomedical applications. [40]

In this regard, it has been shown that SiC/SiO_x core/shell NWs coated with light-absorbing organic molecules (so-called photosensitizers) can be efficiently applied in anti-cancer therapy using X-ray excitation, [40] since the energy absorbed by the X-ray excited inorganic NWs can be efficiently transferred to the photosensitizer that generates highly reactive oxygen species, which in turn have cytotoxic effects. [41]

To exploit the intriguing and remarkable features offered by SiC/SiO_x core/shell architectures, one must characterize accurately their chemical-physical properties, in particular by investigating both the SiO_x outer shell and the SiC/SiO_x buried interface, typically populated by defects, e.g. carbonaceous contaminants, oxycarbides related to the carbide oxidation process, [42] and oxide impurities that can dramatically modify and deteriorate the electrical properties of electronic and optoelectronic devices. [43,44] In this respect, a variety of experimental techniques have been routinely used to determine structural and also chemical properties of the SiC/SiO_2 interface, such as transmission electron microscopy (TEM), [45] photoemission electron spectroscopy (PES) [46–48] and X-ray absorption near-edge spectroscopy (XANES). [49,50] The latter, in particular, revealed to be a powerful tool for investigating nanostructured materials and inner interfaces. [6,51] However, state-of-the-art computational investigations are limited to the crystalline phases of SiC nanowires, [52–56] while the SiC/SiO_x interface is modeled only in the case of geometries as slabs or nanodots. [57,58] Furthermore, these models are not enough accurate and realistic for shedding light on the many electronic and structural information enclosed in XANES spectra, and to explain the absorption peak lineshape of several transitions arising from these structures. In order to obtain a reliable picture for linking structural features to absorption peaks, a full atomistic model of SiC/SiO_x core/shell NWs, including adventitious carbon, defects and contaminants still must be developed. In this work, we thus analyse first the structural arrangements

and composition of SiC/SiO_x core/shell NWs using multiscale modeling; second, we investigate the electronic and optical properties of these nanostructures characterized by various defects and impurities by comparing ab-initio simulations of absorption spectra (XANES) with recorded experimental data on in-house grown NWs to characterize these systems and eventually validate our computational model. This analysis led us to devise a realistic model of SiC/SiO_x core/shell NWs that includes the interface region between the two different materials, that is the amorphous SiO_x shell and the SiC core nanowire. The synergic use of computational and experimental tools delivers a comprehensive and more accurate chemical-physical description of SiC/SiO_x core/shell NWs, paving the way towards their use in power electronics, nanomedicine, and many other applications requiring high endurance.

2 Experimental details

The SiC/SiO_x core/shell NWs were grown via a bottom-up carbothermal method, based on the reaction between carbon monoxide and the native oxide on (001) Si substrates, using iron oxide as a catalyst. [31,36] The core/shell structure of a single NW with diameter of ~ 60 nm is represented in Fig. 1(a), reporting the TEM axial and cross-sectional views. As a reference for the SiC/SiO_x interface (SiC core NWs without shell), the SiO_x was fully removed from the as-grown NWs by etching the substrates in hydrofluoric acid (HF) (1 : 3) aqueous solution for an extended period of 60 min. NWs without SiC core (denoted as SiO_x NWs) were grown by omitting the carbon monoxide precursor and are used as a reference for SiO_2.

Synchrotron measurements were performed at the BEAR beamline (BL8.1L) of the ELETTRA synchrotron facility (Italy) and at the Spherical Grating Monochromator (SGM) beamline of the Canadian Light Source, University of Sasketchewan (Canada). The BEAR beamline provides a photon energy range of $3 - 1600$ eV with a resolution of E /Δ E ~ 3000 and an incident photon flux (i.f.) of $\sim 1 \times 10^9$ photons/s for C K-edge studies, whereas the SGM beamline provides a photon energy range of $250 - 2000$ eV with the resolution of $E/\Delta E \sim 5000$ for Si K-edge (i.f. $\sim 1 \times 10^{11}$ photons/s) and O K-edge (i.f. $\sim 1 \times 10^{12}$ photons/s) measurements. XANES spectra were collected from all three types of NWs, i.e., as-grown SiC/SiO_x core/shell, SiO_x and HF-etched SiC NW ensembles that were maintained on the planar substrates.

The spectra were collected in total electron yield (TEY) mode (i.e., drain current mode) in the energy range $270 - 320$ eV, $510 - 570$ eV and $1830 - 1880$ eV corresponding to the C, O and Si K-edge, respectively. XANES data were normalized to the corresponding spectrum acquired on a photodiode at the end of the beamline. The energy scale of each single spectrum was re-calibrated taking into account the energy fluctuations of characteristic absorption features measured on the refocusing mirror and Au mesh, respectively.

3 Computational details

3.1 Modeling of SiC and SiC/SiO$_x$ core/shell NWs

The steps performed to obtain a fully realistic model of SiC/SiO$_x$ core/shell NWs, similar to the typical structure shown in Fig. 1(a), are the following: generation of the pristine SiC NW core, passivation of the SiC NW surface with different chemical elements, and creation of the SiO$_x$ outer shell by embedding the SiC core. These three steps are described one by one in the following sections.

3.1.1 Structure of the SiC core

The SiC nanowires (NWs) were obtained by cleaving a cylinder out of a 3C-SiC supercell along the [111] direction, which represents the growth axis in our synthesis process. In particular, using a cubic cell with lattice parameter $a = 4.348$ Å for the 3C-SiC crystal structure, one obtains a simulation supercell for the NW with an axial periodicity of $a\sqrt{3} = 7.5309$ Å. The z direction identifies the cylindrical symmetry axis of the NW (the cylindrical symmetry is removed by molecular adsorption). The size of the calculation supercell was chosen equal to 50 Å in the transverse direction, that is large enough to avoid spurious interactions between periodic images, even in the case of the NWs with the largest diameter (26 Å). Pristine SiC NWs are forcefully characterized by the presence of contaminants at the surface. The latter dramatically modify the electronic and optical properties of these nanosystems.[59,60] In the following section we thus thoroughly assess these effects.

3.1.2 Surface passivation of the SiC core

Surface-related states have a large impact in systems at nanoscale and appear usually as intra-gap states.[54] In particular, the terminations of the dangling bonds present on the SiC NW surface can affect dramatically the electronic structure and, thus, must be carefully investigated.

To perform the analysis of possible surface contaminants, we have saturated the dangling bonds of C and Si superficial atomic centers by using different atomic species and chemical compounds, notably −H atoms and hydroxyl groups (−OH). Indeed, oxidized OH-SiC NWs can help our understanding of the SiC core/SiO$_x$ shell interface in the HF-etched SiC NW samples, which consists of a thin layer of silicon oxycarbides.[36]

	Band Gap (eV)	
Radius (nm)	−*H* sat.	−*OH* sat.
0.6	*3.30*	*2.55*
0.9	*2.79*	*2.10*
1.3	*2.52*	*2.05*

Table 1 Band gap of the SiC core NW terminated with −H atoms or −OH radicals as computed by DFTB.

The optimized configurations of these saturated NWs were obtained by using the Self-Consistent Charge Density Functional Tight Binding (SCC-DFTB) approach, implemented in the DFTB+ code suite.[61] To perform the DFTB structural and electronic relaxations we used the Slater-Koster parameter set *matsci-0-3*[62] and we included the *d*-orbitals in the local basis set of the silicon
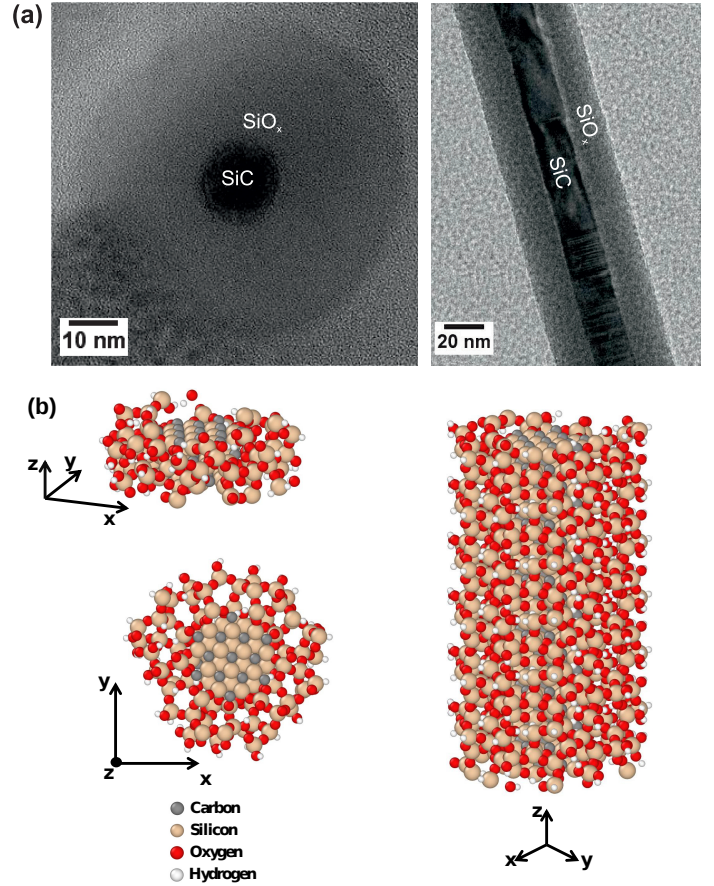

Fig. 1 (a) TEM images adapted from Refs.[36,63] of a SiC/SiO$_x$ core/shell NW in axial view (left panel) and cross-sectional view (right panel). b) Computational model of a single SiC/SiO$_x$ core/shell NW; left panel shows the NW unit cell side view (upper part) and top view (lower panel); right panel shows a side view of the NW supercell obtained by periodically repeating the unit cell along the rotational symmetry axis direction.

atoms, which are essential to achieve accurate band gap and band structure (for further detail see ESI †(sub-s 1.1)). Electronic structure simulations were carried out in the unit cell using a $1 \times 1 \times 4$ *k*-point grid sampling. Forces among all atoms within the supercell are relaxed below 0.05 eV/Å.

In agreement with previous ab-initio studies,[54] we find that the −OH termination is stable at the surface of the NW. This configuration is more stable than that one with unsaturated O atoms; moreover, −OH impurities are preferentially anchored to the Si atom at the surface, presenting formation energies of 1.76 and 3.82 eV for the C-OH and Si-OH configuration, respectively.[54]

In the case of −H passivation the band gap decreases by increasing the size of the radius, and tends asymptotically to the bulk value, which from our calculations is 2.3 eV (experimentally the band-gap of crystalline 3C-SiC is 2.36 eV[64]). We notice that the band gap for a 1.2 nm diameter NW is 3.3 eV (see Tab. 1). This value is rather different from the one obtained by using the full density functional (DFT) approach, which is 2.7 eV, in agreement with previous DFT simulations.[54,55] Nevertheless, this difference is consistent with the value of the 3C-SiC Γ point energy gap (which is larger than the fundamental band gap) found to be 1.41

eV from full DFT calculations. DFTB band-gap (2.3 eV), possibly because of the Slater-Koster parametrization, is very much close to the measured band gap (2.36 eV) with respect to that obtained by DFT. These findings make us confident that DFTB can be safely used to describe the chemical-physics of the SiC NWs. By passivating the superficial dangling bonds of the SiC NW with $-OH$ we find a similar behaviour of the band gap, monotonically and asymptotically decreasing with the increasing diameter (see Tab. 1).

The major finding of our electronic band structure simulations (see Figs. S7 and S9 of ESI †for the NWs' band structure) is that both H-SiC and OH-SiC NWs turn into a direct band-gap semiconductor, with the minimum distance between the valence band maximum (VBM) and the conduction band minimum (CBM) at the Γ point. This change is basically due to electron quantum confinement obtained by reducing the system dimensionality from 3D to 1D. Nevertheless, the band-gap calculated for the two terminations is rather different at the same radius (see Tab. 1), that is consistently lower in the case of $-OH$ termination.

This difference can be rationalized in terms of both chemical termination and quantum confinement. Indeed, these two effects compete with each other and affect the electronic behaviour of the nanosystem. Quantum confinement tends to increase the band gap and largely influences systems mostly at the nanoscale, as asymptotically the band gap must match the bulk value of 3C-SiC almost independently of the surface termination. At small radius, we find that the Mulliken charge distribution of the atoms close to the surface is rather homogeneous in the case of $-H$ termination, while using $-OH$ passivation the superficial atoms are partially deprived of their charge due to the high electronegativity of oxygen atoms (see ESI †(sub-s 1.1)). Thus, surface states are more likely to appear and to affect more significantly the $-OH$ terminated SiC NW, reducing the band gap with respect to the $-H$ passivated NW. Furthermore, we find that the band gap of the oxidized OH-SiC NWs is free from defective states and that the OH-SiC NWs are non-magnetic systems (see Fig. S6 of ESI †). To reinforce our conclusions on the effects induced by different passivations of the NW surface, drawn on the basis of the Mulliken charge population analysis, we notice that also the calculation of the HOMO and LUMO probability densities (square modulus of the wavefunctions) of the H-SiC and OH-SiC NWs may shed some light on the chemical-physical modifications leading to the measured XANES spectral line shape. Thus, in Figures S10 and S11 of the ESI †we plot the VBM and CBM real-space probability densities for the smallest radius NW. In particular, we notice that in the case of $-H$ terminated NWs both the VBM (left hand side of Fig. S10) and the CBM (left hand side of Fig. S10) are localized in the core of the NW, while in the case of $-OH$ termination the VBM (left hand side of Fig. S11) is localized on the oxygen atoms and the CBM (right hand side of Fig. S11) remains mostly core-localized. This different spatial distribution of the CBM and VBM can be attributed to the strong electronegativity of the oxygen atomic species.

In the following simulations we decided to use the 0.6 nm radius SiC NW, due to the high computational cost for treating larger wires. Furthermore, due to the fact that XANES is a probe of the local environment, we expect that this model system is sufficient to reproduce accurately XANES experimental data.

3.1.3 SiC/SiO$_x$ core/shell nanowire

The amorphous SiO$_x$ outer shell was built above the 0.6 nm radius SiC core by using molecular dynamics (MD) with reactive potentials (ReaxFF[65]). In particular, the parametrization of the forces has been chosen[66] to reproduce SiO$_x$ and SiC structures at different stoichiometry. To perform these simulations we used the LAMMPS code.[67] The interface between SiC and SiO$_x$ was
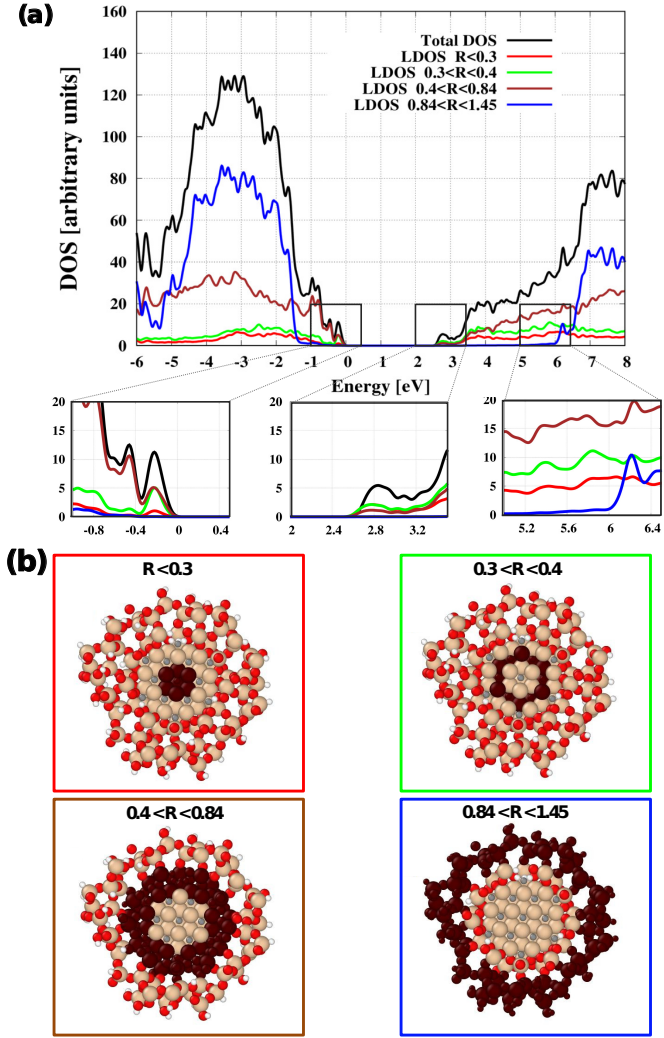

Fig. 2 (a) DOS of our computational model of SiC/SiO$_x$ core/shell NW; the upper panel (a) shows both the total Density of States (black line) and the local DOS (LDOS) obtained by projecting the DOS onto the atoms belonging to different radial shells; the three middle panels report zooms of the top (bottom) region of the valence band (conduction band); (b) NW radial shells (represented in dark brown) on which the DOS projections are performed.

created by saturating the C and Si dangling bonds protruding from the surface of the SiC NW core with oxygen atoms, and by adding Si-O groups in order to have Si tetrahedrally coordinated with oxygen atoms (see Fig. S12 of ESI †(sub-s 1.2) for further details). In this way the number of bonds at the interface

is decreased by a factor 2.3 to better match the density of stoichiometric SiO_2. Finally, a MD run was performed to optimize and rearrange the outer shell atomic configurations, while the remaining dangling bonds were saturated by means of hydrogen atoms. The final structure of the model SiC/SiO_x core/shell NW, reported in Fig. 1(b), has been further characterized with respect to bond lengths and relative angle distributions, finding a good agreement with the literature (for more details about structural modeling and characterization see ESI †(sub-s 1.2) and †(sub-s 1.3), respectively).

3.2 Electronic structure simulations of the SiC/SiO_x core/shell nanowire

The SiC/SiO_x core/shell NW model has been characterized by computing the electronic band structure and the DOS using SCC-DFTB. In Fig. 2(a) we report both the total DOS and the local DOS (LDOS) obtained by projecting onto the atoms belonging to different radial shells, which are represented in dark brown in Fig. 2(b).

We notice that the LDOSs reproduce unambiguously the different NW building blocks. Indeed, for $R \leq 0.4$ nm, which means within the NW core, both the LDOS (red and green curves in Fig. 2(a)) and the band gap correspond to those of a SiC NW; for $R \geq 0.84$ nm the LDOS and the band gap are related to those of amorphous SiO_x (blue curve in 2(a)); finally for R in the range $0.4 - 0.84$ nm, corresponding to the interface region, we find a shape of the LDOS (brown curve in Fig. 2(a)) intermediate between the SiC core and the SiO_x shell (i.e. VBM reminds that of SiO_x, whereas the CBM resembles that of SiC).

3.3 Simulations of XANES spectra

XANES experimental spectra were reproduced from ab-initio simulations using density functional theory. To perform these calculations we used the XSpectra computer code,[68] which relies on the QUANTUM ESPRESSO suite.[69] The input of the approach implemented in XSpectra is basically the ground state electron density. K-edge absorption spectra are computed upon the knowledge of the electron density via the continued fraction method and the Lanczos chain algorithm, tailored to be used with pseudopotentials.[68] The convenience of using this approach is mainly due to its low computational cost, as it is based on one only self-consistent DFT run and does not require the explicit calculation of the empty states. The drawback of this method is that one loses useful pieces of information (e.g. symmetry) on the final transition states.

The absorption of X-ray photons results typically in a core-hole, while the electron is promoted to an empty state. To enable the pseudopotential approach, in which core electrons are typically frozen, to describe this mechanism, one needs to perform DFT simulations with pseudopotentials carrying an inner hole, typically in the $1s$ state for K-edge absorption spectroscopy. Ultrasoft core-hole pseudopotentials, used to perform XANES simulations, for treating the ionic core- valence electron interactions in C, O, and Si atoms can be found in the QUANTUM ESPRESSO database.[70] The all-electron wavefunction is then recovered via the projector augmented wave (PAW) formalism.[71] In particular, for the C pseudopotential we used two projectors on the s and p atomic states, while for Si and O we used two projectors for the s and p states and one for the d state. After convergence tests (details are reported in ESI †(sub-s 2)), DFT simulations have been carried out using a kinetic energy cut-off equal to 544 eV for wavefunctions and four times as much for the electron density. A $1 \times 1 \times 2$ k-point sampling of the Brillouin zone was sufficient to obtain converged energy and DOS below chemical accuracy.

XANES spectra are calculated in the dipole approximation, thus due to symmetry K-edge spectroscopy probes only the transitions from $1s$ to np or s/p-hybridized orbitals. Spectra simulations were performed using a $1 \times 1 \times 4$ k-point grid for sampling the Brillouin zone. Three different polarization vectors of the incident light were considered, that is one along the NW symmetry axis (z-axis) and two perpendicular to it (x and y directions). A dependence of the spectral signals on polarization directions is expected in presence of radial anisotropy, e.g. for defected NWs. In all XANES simulations spectral lineshapes have been broadened by a convolution with a Lorentzian function having the half width at half maximum constant at all energies and equal to 0.8 eV.

Numerical tests were carried out in the case of SiC crystals and of SiC NW with −OH terminations. Good agreement of our calculations with experimental measurements and similar computer simulations[52,54] on these structures was found using the above-mentioned computational parameters. These encouraging results on SiC NW led us to use the model of SiC/SiO_x core/shell NW previously introduced to interpret our experimental absorption data. More computational details on XANES simulations are reported in ESI †(sub-s 2.1).

4 Results and Discussion

4.1 Silicon K-edge XANES spectra

Before investigating the Si, O, and C K-edge absorption lineshape of the SiC/SiO_x core/shell NW, we start our analysis by simulating the electronic and optical properties of the OH-terminated SiC core. This configuration represents a simplified model of the SiC core NW, which can be experimentally obtained by completely etching away the silica outer shell (HF-etched SiC NWs). In Fig. 3 we report the theoretical Si K-edge spectrum (black dashed line) in comparison to our experimental data (red line). Furthermore, in this figure we report the spectral contribution to the total lineshape of the light polarized along the three orthogonal cartesian directions: the blue, khaki, and green curves show the spectra originating from x-, y-, and z-polarized electric fields, respectively. The total spectrum is obtained by averaging along the three polarization directions. The experimental lineshape of the Si K-edge exhibits five features A–E that are typically observed for 3C-SiC thin films[72–74] and HF-etched 3C-SiC NWs.[52,75] Differently to previous reports, we observe an additional feature B* at 1847 eV that becomes only visible when the freshly etched sample was immediately inserted into the UHV chamber. Longer exposure to air leads to the disappearance of this feature (see Fig. S20a of ESI †), suggesting that it originates from the SiC/SiO_x interface (i.e., before any re-oxidation appears). We notice that the simulated
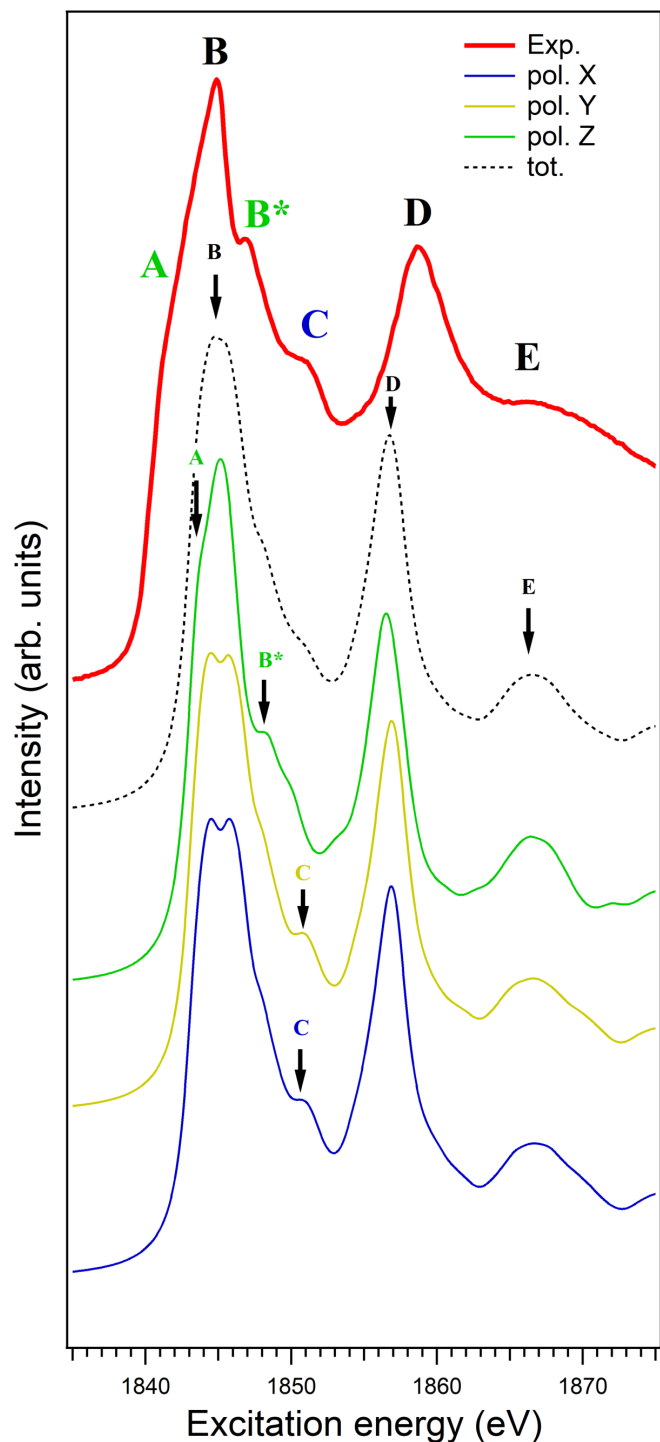
Fig. 3 Experimental Si K-edge XANES spectrum of HF-etched SiC core nanowires (red), in comparison with theoretical XANES spectra of (dashed line) an OH-terminated SiC core NW. Blue, khaki, and green curves show the spectra originating from x-, y-, and z-polarized electric fields, respectively.

spectra are in good agreement with experiments, and they reproduce all the peaks denoted in Fig. 3. It is noteworthy that the shoulder A (at 1841.5 eV in the experimental spectrum) strongly depends on the polarization direction: it is well separated from the main peak B for x- and y-polarized electric fields, whereas it decreases in intensity and appears as shoulder for z polarization direction. Moreover, peak B* is more pronounced in the spectrum with the z-polarized electric field. Overall, the theoretical spectral lineshape in the z polarization direction agrees well with the experimental one.

The peaks denoted as B, D, and E in Fig. 3 correspond to transitions from the Si1s orbital to hybridized states from both Si and C. In particular, the main resonance (B peak at 1845 eV), and the peaks D and E at 1849 and 1867 eV, respectively, can be attributed to the transition of Si1s electrons to orbitals that have lost their atomic character and arise by mixing hybridized 2s and 2p orbitals of C and hybridized 3s, 3p, and 3d orbitals of Si.[75] This combination is due to the overlap between 3s, 3p, and 3d orbitals from Si and 2s and 2p orbitals from C, which are degenerate as one can clearly see in Fig. S6 of the ESI †.

Theoretical interpretation of the Si K-edge absorption spectra has been carried out by comparison with our experimental measurements also in the SiC/SiO$_x$ core/shell NW. Both simulated and experimental Si K-edge spectra, along with the contributions resolved in the polarization directions of the incident electric field, are reported in Fig. 4. Si atoms in different chemical environments are present in the SiC core as well as in the SiO$_x$ outer shell. Thus, theoretical spectra were obtained by creating core-holes in two different locations of the NW. In Fig. 4 the K-edge spectrum obtained via photon absorption by Si atoms within the outer shell of the NW is labeled as Si$_h^{shell}$ (black dashed line in the upper part of the figure), while the spectrum labeled as Si$_h^{core}$ (black dashed line in the lower part of the figure) has been generated by creating the core-hole in the Si atoms within the NW SiC core. The Si$_h^{shell}$ spectrum reports the features typical of silica, that is a single main peak C' (see also Fig. S16b of ESI †).[68] At variance, the Si$_h^{core}$ absorption spectrum is similar to that one obtained in the SiC+OH NW (see Fig. 3). The pre-edge peak labeled as A' at 1842 eV in the experimental spectrum in Fig. 4 can be unambiguously attributed to a contribution stemming from the SiC core, since it cannot be found in the SiO$_x$ NWs without SiC core (see Fig. S20b of ESI †). In general, the spectral lineshape can be rationalized as the convolution of the signals obtained by creating the core-hole in different locations in the SiC core and in the SiO$_x$ outer shell. Nevertheless, a much stronger contribution of the Si$_h^{shell}$ is visible. Taking into account this feature, which can be understood by considering that the TEY experimental technique probes mainly the sample's surface, good agreement is obtained between experimental (red line) and theoretical spectral lineshape. Similar to Fig. 3, the shoulder B' at 1845.5 eV is strongly dependent on the polarization direction (i.e., more pronounced for x- and z-polarized electric fields), and the spectral lineshape of the experimental data is mainly dominated by the theoretical one of the Si$_h^{shell}$ in z polarization direction. We notice that the main peak C' in Fig. 4 (at 1847 eV) is largely due to electron transitions from Si1s to a combination of Si3p,3d orbitals,
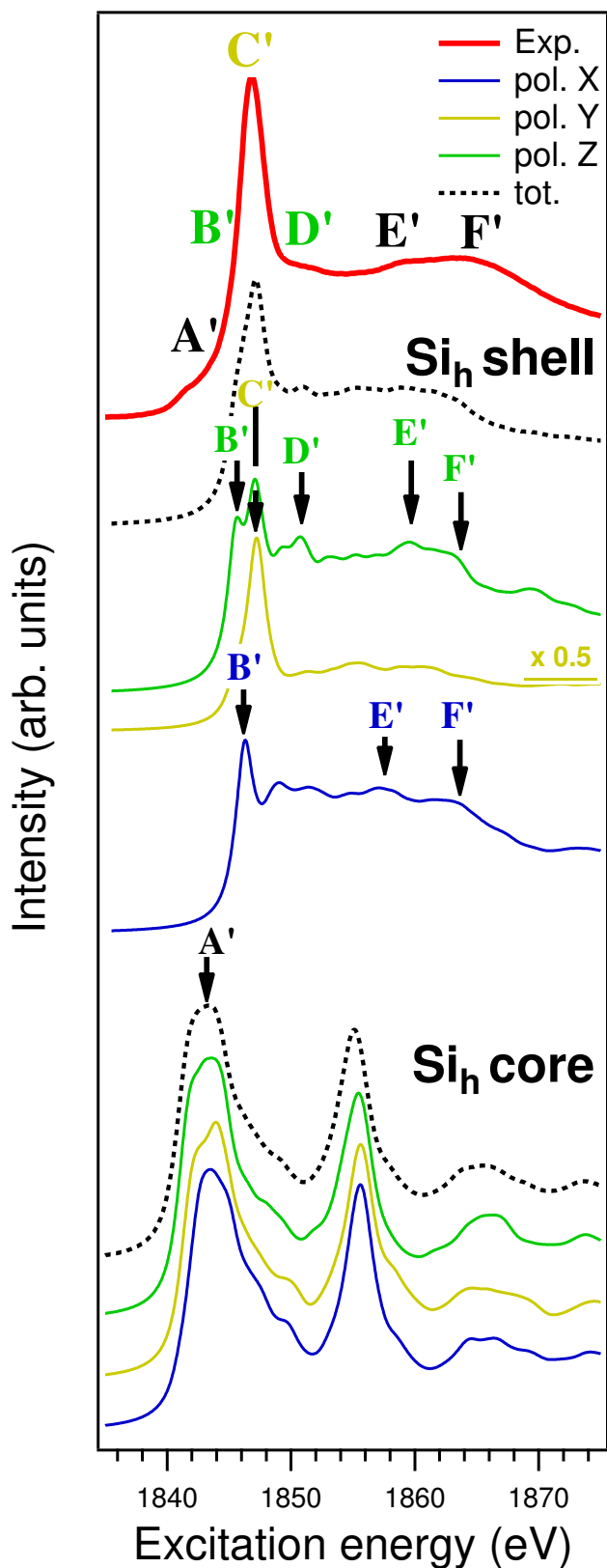
Fig. 4 Experimental Si K-edge XANES spectrum of as-grown SiC/SiO$_x$ core/shell NWs (red), in comparison with theoretical XANES spectra (dashed line) of a SiC/SiO$_x$ core/shell NW (without carbon defects). Si$_h^{shell}$ and Si$_h^{core}$ represent the absorption spectra obtained by creating a core-hole in a silicon atom within the SiO$_x$ shell and the SiC core, respectively. Blue, khaki, and green curves show the spectra originating from x-, y-, and z-polarized electric fields, respectively.

due to the selection rules (see Fig. S6 of ESI †for a symmetry-resolved representation of the DOS).

4.2 Oxygen K-edge XANES spectra

The comparison between the theoretical O K-edge XANES spectra (black dashed lines) obtained in our SiC core+OH model NW and the experimental O K-edge XANES spectrum of HF-etched SiC core NWs (red line) is reported in Fig. 5. In all simulated spectra blue, khaki, and green curves show the features originating from x-, y-, and z-polarized electric fields, respectively. The two theoretical spectra (black dashed lines) in the upper and middle parts of Fig. 5, labeled as $-$Si-O$_h$H and $-$C-O$_h$H, correspond to spectral features originating from different locations of the excited O atom on the NW surface: on the one hand, O binds to Si ($-$Si-O$_h$H), and on the other hand to C ($-$C-O$_h$H). We notice that good agreement between experimental and theoretical data is found, with the main features fully described by ab-initio simulations using our NW model. In particular, the main peak 3 at 536 eV is present in both simulated spectra $-$Si-O$_h$H (x-polarization) and $-$C-O$_h$H (x- and y-polarization), whereas the shoulder 2 at 534 eV and the features 4, 5 and 6 (at 540, 544 and 557 eV) are only reproduced by the $-$Si-O$_h$H simulated spectra (contributions from y- and z-polarization).

Finally, in the lower part of Fig. 5 we report the spectrum, labeled as $-$C=O$_h$, simulating the presence of unsaturated oxocarbons (carbonyl groups) on the SiC NW surface. The lineshape, originating from O atoms that form double covalent bonds with the adjacent carbon atom, explains the pre-edge peak at 530 eV denoted by 1 in the experimental spectrum (red line). The peaks in all spectra can be described in terms of electron excitations from the O1s orbital to a mixing between hybridized 2s,2p orbitals of C or 3s,3p orbitals of Si and the 2s,2p orbitals of O.

In Fig. 6 we report the comparison between experimental (red line) and simulated (black dashed line) O K-edge XANES spectra of the SiC/SiO$_x$ core/shell NW. In addition, the lower part of Fig. 6 shows the simulated spectra of $-$C=O$_h$ carbonyl groups on the NWs' silica surface. The main features $2'-6'$ of the experimental spectrum are all clearly visible in the theoretical spectrum without carbon defects, when the different polarization contributions are summed up (blue, khaki, and green curves show the spectra originating from x-, y-, and z-polarized electric fields, respectively). This finding further supports our computational model of the SiC/SiO$_x$ core/shell NW. In particular, the main broad peak in the energy range 535-540 eV is split into two separate contributions, namely into peak 2' at 535 eV originating from the $y-$ (khaki line) and $z-$ (green line) polarization directions of the incident light, whereas peak $3'$ at 537 eV originates from the $x-$ (blue line) polarization direction. Moreover, the shoulder $4'$ visible at 541 eV is recovered by convolution of features present in all the polarization directions x,y and z. The broad features $5'$ and $6'$ found in the experimental spectrum at 552.5 and 558 eV, respectively, are present in all the three polarization directions of the simulated spectra, but its lineshape can be mainly understood by looking at the lineshape of the y-polarization contribution (khaki curve).
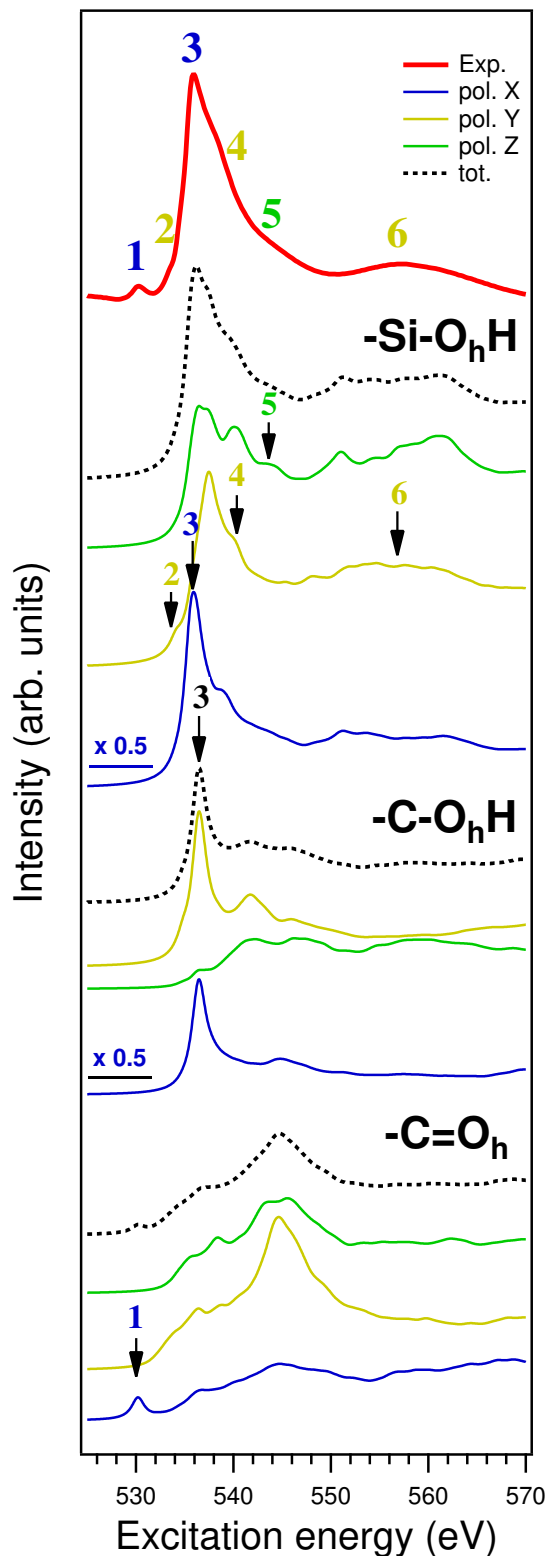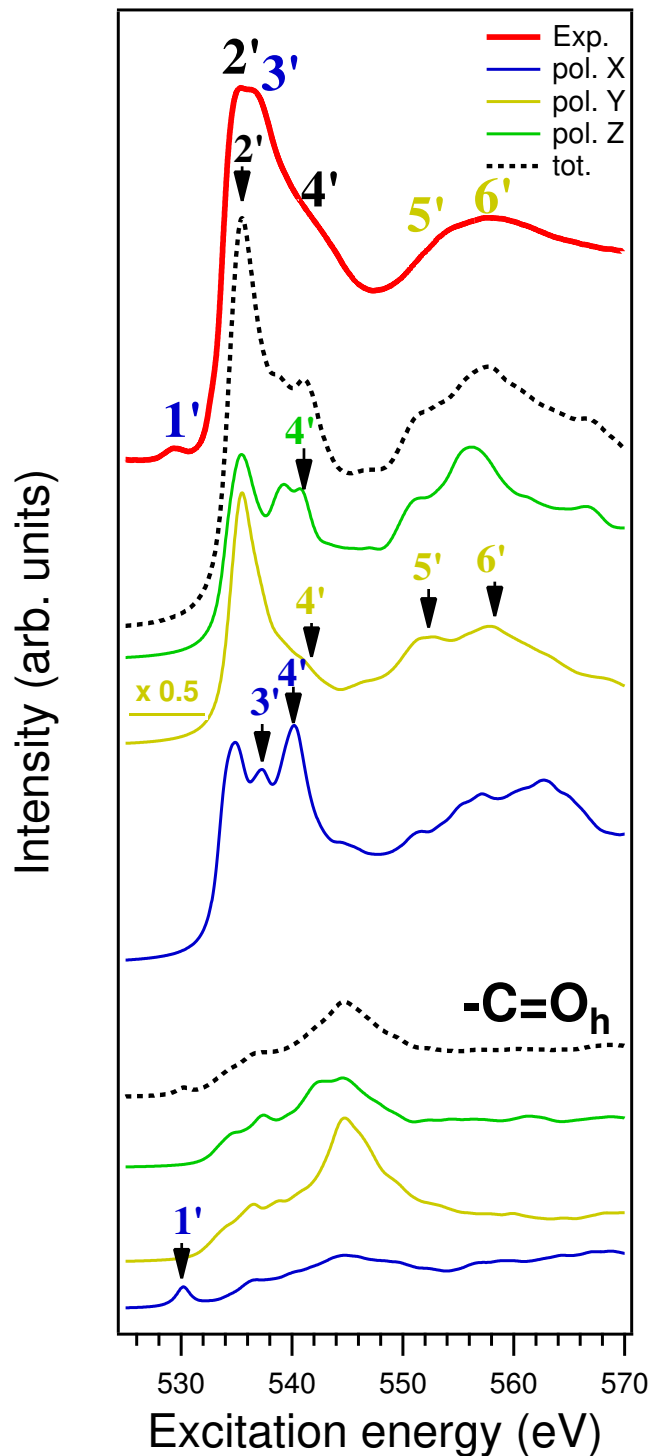
Fig. 5 Experimental O K-edge XANES spectrum of HF-etched SiC core nanowires (red line), in comparison with theoretical spectra of an OH-terminated SiC core NW (black dashed lines). The three theoretical spectra with the relevant polarizations (blue, khaki, and green curves show the spectra originating from x-, y-, and z-polarized electric fields, respectively) refer to the -OH radicals attached to a silicon atom (upper theoretical spectrum), to a carbon atom (middle theoretical spectrum), and to unsaturated oxygen (lower theoretical spectrum).

Fig. 6 Experimental O K-edge XANES spectrum of as-grown SiC/SiO$_x$ core/shell NWs (red), in comparison with theoretical spectra (black dashed line) of a SiC/SiO$_x$ core/shell NW (without carbon defects). In the lower panel we report again the spectral features originating from unsaturated oxygen. Blue, khaki, and green curves show the spectra originating from x-, y-, and z-polarized electric fields, respectively.

A similar experimental lineshape of the O K-edge XANES spectrum, i.e., a relatively broad resonance between $535 - 550$ eV, but no pre-edge peak 1' was previously observed in a SiO_2 thin film (4 nm) thermally oxidized on SiC[50] as well as in thermally oxidized Si NWs.[76] At variance, our SiO_x NWs (grown without SiC core) exhibit the same pre-edge peak at 530 eV (see Fig. S21 of ESI †) than the SiC/SiO_x core/shell NWs. It is noteworthy that a different view about the origin of the pre-edge peak $1/1'$ in O K-edge XANES spectra of SiO_x-based materials exists in the literature. For instance, in SiO_x films grown on SiC it has been assumed that it originates from defect states such as O vacancies at the SiO_x/SiC interface.[48] Furthermore, a similar pre-edge peak has been observed in quartz,[77] which has been assigned to the transition from the O1s electron to the π^* orbital states of O_2 molecules that are induced by radiation damage from the X-ray beam with high incident flux.[78] At odds with this theory, we could observe the pre-edge peak even during acquisition at very low flux (at BEAR beamline, i.f. $< 1 \times 10^9$ photons/s, see Fig. S17 of ESI †), thus, we can exclude any effects caused by radiation damage. As in the case of O K-edge spectrum of HF-etched SiC core NW (see Fig. 5) the pre-edge peak 1' located at 530 eV in Fig. 6 can be safely attributed to double bonded oxygen, e.g. belonging to carbonyl groups (see simulated spectra of $-C=O_h$ in the lower part of Fig. 6). To further confirm this theory, we measured the O K-edge XANES spectrum of NWs after surface functionalization with an organic molecule containing carboxyl groups (see Fig. S17 of ESI †). Indeed, we found an increase of the pre-edge peak, supporting the idea that it originates from carbon-containing (functional) groups such as carbonyl and/or carboxyl groups.[79]

4.3 Carbon K-edge XANES spectra

The comparison between the C K-edge XANES simulated spectrum of OH-terminated SiC core NW (black dashed line) and the experimental spectrum of HF-etched SiC core NWs (red line) is reported in Fig. 7. The color code for the three orthogonal polarization directions of the incident X-ray photon beam is the same as for the previously discussed Si and O K-edge XANES spectra. To consider contributions stemming from the SiC/SiO_x interface, we simulated a typical carbon-related defect (lower part of Fig. 7). In principle, this structure is created when a Si atom in SiO_x is substituted by a C atom, and resembles a C atom in sp^3 configuration corresponding to SiO_xC_y species (i.e., silicon oxycarbides indicated as grey-shaded area in the structure in Fig. 7), which are typically resistant to HF etching. We notice that the clusters represented in Figs. 7 and 8 were cut out of the full simulation cell with the only aim of zooming the several chemically different local environments in which carbon atoms can be found in their binding to others atoms. These realistic binding conditions of the carbon atoms within the different clusters, which are embedded in the NW, are then used to disentangle the spectral contributions of the single defects to the total lineshape. Nevertheless, XANES spectra are calculated on the full simulation cell.

Our experimental lineshape of the C K-edge XANES spectrum is in good agreement with previous reports for 3C-SiC thin films[80–82] and HF-etched 3C-SiC NWs.[52,75] Apart from the first
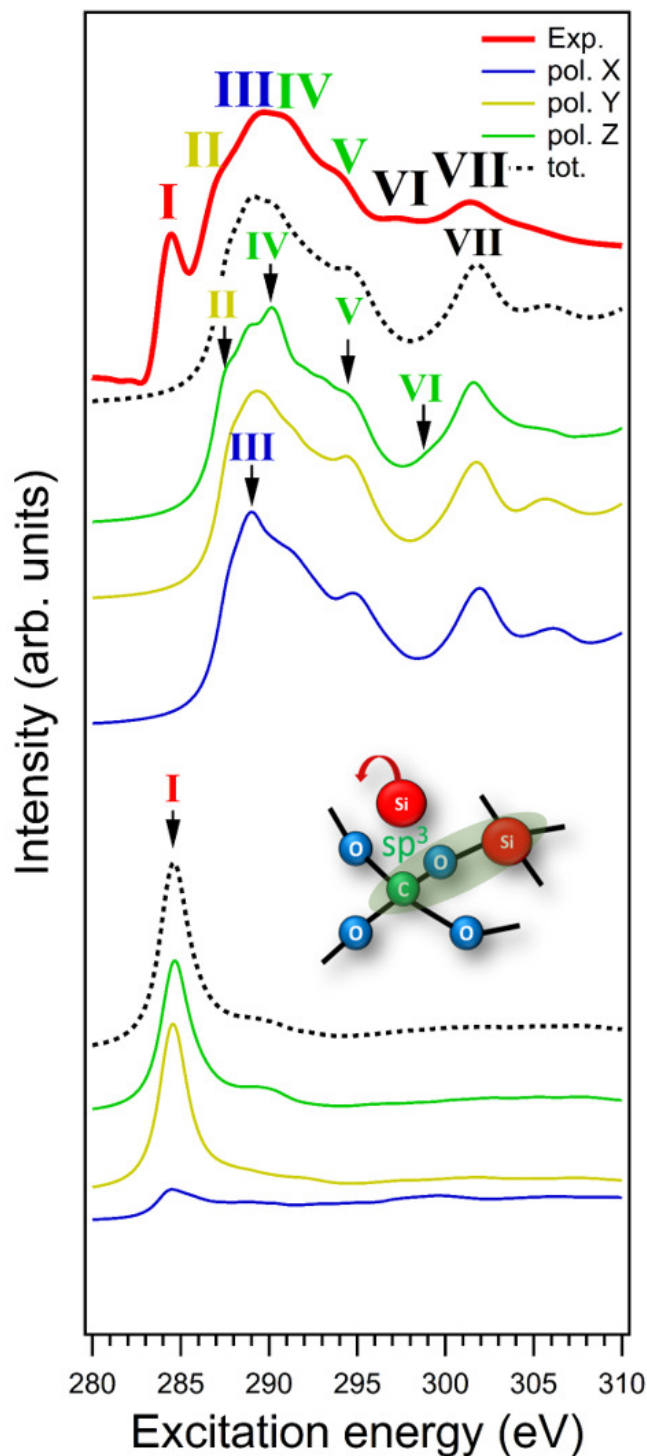

Fig. 7 Experimental C K-edge XANES spectrum of HF-etched SiC core NWs (in red), in comparison with theoretical spectra (black dashed line) of an OH-terminated SiC core NW. The simulated spectra in the lower panel refer to residual silicon oxycarbides (grey-shaded area in the structure) that remain as residuals at the SiC surface after etching the SiO_x shell. Blue, khaki, and green curves show the spectra originating from x-, y-, and z-polarized electric fields, respectively.

9

feature I located at 284.5 eV, the theoretical spectrum (without defects) reproduces well the experimental shape. In our model of SiC core NW with $-OH$ termination, C atoms that are not on the surface form sp^3 hybridized orbitals bonding with Si atoms. We assign the spectral features in the near edge region (energy range between 285 and 300 eV) to the dipole transitions from the C1s orbitals to σ^*-character bands formed by the sp^3-hybridized orbitals of C, tetrahedrally coordinated with four Si atoms.[52] At variance, the pre-edge peak I can be attributed to the transition from the (sp^3) C1s atoms at the SiO$_x$/SiC interface (see lower panel in Fig. 7), where a layer of silicon oxycarbides is typically formed due to the growth process and conditions and remains as residual thin $(0.5 - 2$ nm) layer around the SiC core.[36]

It is noteworthy, that such a pre-edge peak I has been previously assigned in (HF-etched) 3C-SiC NWs to graphite-like π^* states of sp^2 bonded carbon atoms.[75] Although we cannot exclude any contributions from C atoms in sp^2 configuration, our recent findings strongly suggest that a strong contributions originates from the silicon oxycarbides (in sp^3 configuration) present at the SiO$_x$/SiC interface.

Finally, in Fig. 8 we report the C K-edge XANES theoretical spectra of the SiC/SiO$_x$ core/shell NW (black dashed lines) compared to our experimental data (red line). Here we report four different simulated spectra corresponding to different chemical environments, and thus different bonding, in which C atoms can be reasonably found[20]. Special emphasis was drawn to simulate C atoms not only in sp^3 but also in sp^2 configuration, since additional peaks in the C K-edge XANES spectrum of SiC/SiO$_x$ core/shell NWs have been associated to sp^2 C defects present in or on the silica shell,[52] similar to the SiC case. The different coordination bonds are represented close to the corresponding XANES spectrum in Fig. 8.

The upper theoretical spectrum in Fig. 8 (a) is obtained when an oxygen atom in the SiO$_x$ shell is substituted by a carbon atom, i.e., a sp^3 configuration very similar to that reported in Fig. 7 (upper panel) for the $-OH$ terminated SiC NW. The presence of additional different C defects corresponding to the three lower spectra (b)-(d) in Fig. 8 could be explained by the carbothermal process used in the present study to synthesize the SiC/SiO$_x$ core/shell NWs, which inevitably creates C inclusions/contaminants in the SiO$_x$ shell. The additional defects studied in this work can be divided in two classes, namely substitutional inclusions and surface contaminants. Within the first class belongs the substitution of an oxygen atom in the shell with a $-CH$ group (sp^2 configuration, see Fig. 8(b)), the substitution of a Si atom in the shell with two C atoms forming a double bond (sp^2 configuration, see Fig. 8(c)), and the substitution of a silicon atom in the shell with a four coordinated carbon atom (sp^3 configuration, see Fig. 8(d)), similar to the case in Fig. 7 (lower panel). The second class of defects is characterized by the surface contamination of carboxyl group (the relevant spectrum is reported in the ESI †(sub-s 2.3)).

As can be seen, the theoretical spectrum in Fig. 8(a) mainly reproduces the features II'-V' of the experimental spectrum, whereas the shoulder 0' at 283 eV and the main peak I' at 285 eV, respectively, are not present.

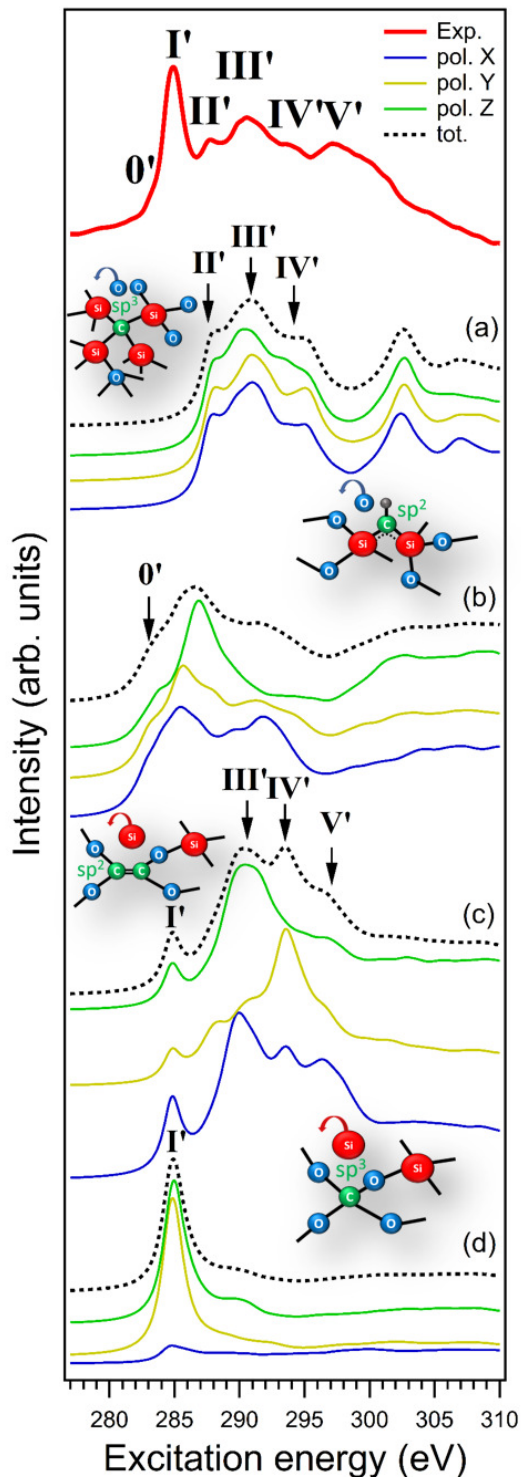However, the theoretical spectrum of the sp^2 configuration (b)

Fig. 8 Experimental C K-edge XANES spectrum of as-grown SiC/SiO$_x$ core/shell NWs (red), compared to theoretical XANES spectra (black dashed line) of SiC/SiO$_x$ core/shell NW. The four spectra reported in this figure are obtained by including several different carbon defects in the shell, which are represented in the right hand side. Spectra originating from x-, y-, and z-polarized electric fields are reported in blue, khaki, and green respectively.

in Fig. 8 indeed reproduces the shoulder 0′, whereas the sp^2 configuration (c) in Fig. 8 contributes to the main peak I'. The spectrum of the sp^3 configuration in Fig. 8(d) is once again composed by a single main peak which gives a strong contribution to peak I'.

Our detailed theoretical analysis for different configurations of the SiC/SiO$_x$ core/shell NWs, while not claiming to be exhaustive, demonstrates that the XANES experimental signals are due to a variety of defects and that spectral lineshapes crucially depend on the local bonding environment of the excited atom, which must be carefully assessed.

5   Conclusions

SiC/SiO$_x$ core/shell NWs are very promising systems in a variety of applications, ranging from energy harvesting to developing novel methods for cancer therapy and diagnosis. To optimize these procedures, an accurate characterization of the electronic and optical properties of these novel structures via a synergic experimental and computational study is necessary. To the best of our knowledge this work is aimed at developing for the first time a realistic model of SiC/SiO$_x$ core/shell NWs, relying on information gained both at experimental and theoretical level.

SiC/SiO$_x$ core/shell NWs were synthesized via a low-cost carbothermal method. Structural features of these NWs were investigated via the acquisition of XANES spectra in TEY mode and their theoretical interpretation from ab-initio simulations. Our NW model, including defected sites and interfacial boundaries between SiC and SiO$_x$, reproduces remarkably well the main features of C, Si, and O K-edge XANES spectra of these structures arranged in several configurations and stoichiometry.

Both optical and electronic characteristics, such as the DOS, of these systems are crucially affected by two counteracting effects, that is quantum confinement and surface termination. Quantum confinement, induced by the reduced dimensionality of the wire with respect to bulk SiC, results into the modification of the NWs band structure from indirect to direct band gap, with a VBM to CBM distance inversely dependent on wire diameter. Surface passivation of the dangling bonds affects both the NW boundaries and the interfacial region. We devised the presence of a variety of defects, such as substitutional C, and different chemical coordination to obtain an overall good agreement between simulated and experimental XANES spectral lineshapes at the Si, O, and C absorption K-edge. This study demonstrates the crucial importance of defective sites in affecting the electronic characteristics of SiC NWs, so to avoid unintentional doping that hinders the development of high-performance SiC-based field-effect transistors.

Finally, the realistic model of SiC/SiO$_x$ core/shell NWs proposed in this combined experimental and theoretical study, being able to deliver an accurate interpretation of the recorded XANES spectra, demonstrates to be a valuable tool towards the optimal design and application of these nanosystems in real devices.

Conflict of interest

There are no conflicts to declare.

Acknowledgements

References

1 P. Reinke, *Inorganic Nanostructures*, Wiley-VCH Verlag & Co. KGaA, Weinheim (Germany), 2012.

2 P. C. Spruijtenburg, J. Ridderbos, F. Mueller, A. W. Leenstra, M. Brauns, A. A. I. Aarnink, W. G. van der Wiel and F. A. Zwanenburg, *Applied Physics Letters*, 2013, **102**, 192105.

3 Y. Ji, Y. Zhai, H. Yang, J. Liu, W. Shao, J. Xu, W. Li and K. Chen, *Nanoscale*, 2017, **9**, 16038–16045.

4 T. D. Ladd, F. Jelezko, R. Laflamme, Y. Nakamura, C. Monroe and J. L. O'Brien, *Nature*, 2010, **464**, 45–53.

5 S. Barth, F. Hernandez-Ramirez, J. D. Holmes and A. Romano-Rodriguez, *Progress in Materials Science*, 2010, **55**, 563–627.

6 J. Zhong, H. Zhang, X. Sun and S.-T. Lee, *Advanced Materials*, 2014, **26**, 7786–7806.

7 N. Fukata, T. Subramani, W. Jevasuwan, M. Dutta and Y. Bando, *Small*, 2017, **13**, 1701713.

8 M. Shao, L. Cheng, X. Zhang, D. D. D. Ma and S.-T. Lee, *Journal of the American Chemical Society*, 2009, **131**, 17738–17739.

9 K.-Q. Peng and S.-T. Lee, *Advanced Materials*, 2011, **23**, 198–215.

10 T. J. Kempa, R. W. Day, S.-K. Kim, H.-G. Park and C. M. Lieber, *Energy & Environmental Science*, 2013, **6**, 719–733.

11 K. Peng, J. Jie, W. Zhang and S.-T. Lee, *Applied Physics Letters*, 2008, **93**, 033105.

12 S. Sim, P. Oh, S. Park and J. Cho, *Advanced Materials*, 2013, **25**, 4498–4503.

13 G. Zheng, F. Patolsky, Y. Cui, W. U. Wang and C. M. Lieber,

Nature Biotechnology, 2005, **23**, 1294–1301.

14 K.-I. Chen, B.-R. Li and Y.-T. Chen, *Nano Today*, 2011, **6**, 131–154.

15 J. L. Coffer, *Semiconducting Silicon Nanowires for Biomedical Applications*, Cambridge : Elsevier Science, 2014.

16 C. R. Eddy Jr. and D. K. Gaskill, *Science*, 2009, **324**, 1398–1400.

17 S. Taioli, G. Garberoglio, S. Simonucci, S. a Beccara, L. Aversa, M. Nardi, R. Verucchi, S. Iannotta, M. Dapor and D. Alfè, *The Journal of Chemical Physics*, 2013, **138**, 044701.

18 R. Verucchi, L. Aversa, M. V. Nardi, S. Taioli, S. A Beccara, D. Alfè, L. Nasi, F. Rossi, G. Salviati and S. Iannotta, *Journal of the American Chemical Society*, 2012, **134**, 17400–17403.

19 L. Aversa, S. Taioli, M. V. Nardi, R. Tatti, R. Verucchi and S. Iannotta, *Frontiers in Materials*, 2015, **2**, 46.

20 F. Devynck, A. Alkauskas, P. Broqvist and A. Pasquarello, *AIP Conference Proceedings*, 2010, **1199**, 108–109.

21 X. Shen and S. T. Pantelides, *Applied Physics Letters*, 2011, **98**, 053507.

22 K. Zekentes and K. Rogdakis, *Journal of Physics D: Applied Physics*, 2011, **44**, 133001.

23 L. Latu-Romain and M. Ollivier, *Journal of Physics D: Applied Physics*, 2014, **47**, 203001.

24 J. Prakash, R. Venugopalan, B. M. Tripathi, S. K. Ghosh, J. K. Chakravartty and A. K. Tyagi, *Progress in Solid State Chemistry*, 2015, **43**, 98–122.

25 Y. Zhang, X. Han, K. Zheng, Z. Zhang, X. Zhang, J. Fu, Y. Ji, Y. Hao, X. Guo and Z. Wang, *Advanced Functional Materials*, 2007, **17**, 3435–3440.

26 P. Hu, S. Dong, X. Zhang, K. Gui, G. Chen and Z. Hu, *Scientific Reports*, 2017, **7**, 3011.

27 R. Wu, K. Zhou, Z. Yang, X. Qian, J. Wei, L. Liu, Y. Huang, L. Kong and L. Wang, *CrystEngComm*, 2013, **15**, 570–576.

28 M. Han, X. Yin, W. Duan, S. Ren, L. Zhang and L. Cheng, *Journal of the European Ceramic Society*, 2016, **36**, 2695–2703.

29 W. M. Zhou, F. Fang, Z. Y. Hou, L. J. Yan and Y. F. Zhang, *IEEE Electron Device Letters*, 2006, **27**, 463–465.

30 S. Z. Deng, Z. B. Li, W. L. Wang, N. S. Xu, J. Zhou, X. G. Zheng, H. T. Xu, J. Chen and J. C. She, *Applied Physics Letters*, 2006, **89**, 023118.

31 M. Negri, S. C. Dhanabalan, G. Attolini, P. Lagonegro, M. Campanini, M. Bosi, F. Fabbri and G. Salviati, *CrystEngComm*, 2015, **17**, 1258–1263.

32 Z. J. Li, H. Y. Yu, G. Y. Song, J. Zhao, H. Zhang, M. Zhang, A. L. Meng and Q. D. Li, *Phys. Chem. Chem. Phys.*, 2017, **19**, 3948–3954.

33 X. Li, J. Huang, J. Lu, Z. Feng, J. Luo and M. Xue, *Journal of Materials Science*, 2017, **52**, 3344–3352.

34 Y. Ryu, Y. Tak and K. Yong, *Nanotechnology*, 2005, **16**, S370–S374.

35 S. Carapezzi, A. Castaldini, F. Fabbri, F. Rossi, M. Negri, G. Salviati and A. Cavallini, *Journal of Materials Chemistry C*, 2016, **4**, 8226–8234.

36 F. Fabbri, F. Rossi, G. Attolini, G. Salviati, S. Iannotta, L. Aversa, R. Verucchi, M. Nardi, N. Fukata, B. Dierre and T. Sekiguchi, *Nanotechnology*, 2010, **21**, 345702.

37 M. Zhang, J. Zhao, Z. Li, H. Yu, Y. Wang, A. Meng and Q. Li, *Journal of Solid State Chemistry*, 2016, **243**, 247–252.

38 J. J. Niu, J. N. Wang and Q. F. Xu, *Langmuir*, 2008, **24**, 6918–6923.

39 F. Fabbri, F. Rossi, M. Melucci, I. Manet, G. Attolini, L. Favaretto, M. Zambianchi and G. Salviati, *Nanoscale Research Letters*, 2012, **7**, 680.

40 F. Rossi, E. Bedogni, F. Bigi, T. Rimoldi, L. Cristofolini, S. Pinelli, R. Alinovi, M. Negri, S. C. Dhanabalan, G. Attolini, F. Fabbri, M. Goldoni, A. Mutti, G. Benecchi, C. Ghetti, S. Iannotta and G. Salviati, *Sci Rep*, 2015, **5**, 7606.

41 R. Tatti, M. Timpel, M. V. Nardi, F. Fabbri, F. Rossi, L. Pasquardini, A. Chiasera, L. Aversa, K. Koshmak, A. Giglia, L. Pasquali, T. Rimoldi, L. Cristofolini, G. Attolini, S. Varas, S. Iannotta, R. Verucchi and G. Salviati, *Mol Sys Des Eng*, 2017, **2**, 165–172.

42 V. Presser and K. G. Nickel, *Critical Reviews in Solid State and Materials Sciences*, 2008, **33**, 1–99.

43 V. V. Afanasev, M. Bassler, G. Pensl and M. Schulz, *Physica Status Solidi (a)*, 1997, **162**, 321–337.

44 S. Dhar, L. C. Feldman, S. Wang, T. Isaacs-Smith and J. R. Williams, *Journal of Applied Physics*, 2005, **98**, 014902.

45 K. C. Chang, J. Bentley and L. M. Porter, *Journal of Electronic Materials*, 2003, **32**, 464–469.

46 Y. Hijikata, H. Yaguchi, M. Yoshikawa and S. Yoshida, *Applied Surface Science*, 2001, **184**, 161–166.

47 P. Soukiassian and F. Amy, *Journal of Electron Spectroscopy and Related Phenomena*, 2005, **144-147**, 783–788.

48 D.-K. Kim, K.-S. Jeong, Y.-S. Kang, H.-K. Kang, S. W. Cho, S.-O. Kim, D. Suh, S. Kim and M.-H. Cho, *Scientific Reports*, 2016, **6**, 34945.

49 C. McGuinness, D. Fu, J. E. Downes, K. E. Smith, G. Hughes and J. Roche, *Journal of Applied Physics*, 2003, **94**, 3919–3922.

50 M. Tallarida, R. Sohal and D. Schmeisser, *Superlattices and Microstructures*, 2006, **40**, 393–398.

51 R. E. Medjo, B. T. Sendja, J. M. Mane and P. O. Ateba, *Physica Scripta*, 2009, **80**, 055602.

52 L. Liu, Y. M. Yiu, T. K. Sham, L. Zhang and Y. Zhang, *The Journal of Physical Chemistry C*, 2010, **114**, 6966–6975.

53 A. Laref, N. Alshammari, S. Laref and S. J. Luo, *Dalton Trans.*, 2014, **43**, 5505–5515.

54 E. Rosso and R. Baierle, *Chemical Physics Letters*, 2013, **568-569**, 140 – 145.

55 Z. Wang, M. Zhao, T. He, H. Zhang, X. Zhang, Z. Xi, S. Yan, X. Liu and Y. Xia, *The Journal of Physical Chemistry C*, 2009, **113**, 12731–12735.

56 R. Rurali, *Phys. Rev. B*, 2005, **71**, 205405.

57 W. Li, J. Zhao and D. Wang, *Solid State Communications*, 2015, **205**, 28 – 32.

58 M. Vörös, A. Gali, E. Kaxiras, T. Frauenheim and J. M. Knaup, *Physica Status Solidi (b)*, 2012, **249**, 360–367.

59 M. Vörös, P. Deak, T. Frauenheim and A. Gali, *Applied Physics Letters*, 2010, **96**, 051909.

60 D. Beke, T. Z. Jánosi, B. Somogyi, D. A. Major, Z. Szekrényes, J. Erostyák, K. Kamarás and A. Gali, *The Journal Of Physical Chemistry (c)*, 2016, **120**, 685–691.

61 B. Aradi, B. Hourahine and T. Frauenheim, *Journal of Physical Chemestry*, 2007, **111**,.

62 T. . G. S. J. Frenzel, A. F. Oliveira N. Jardillier, *TU-Dresden*, 2004-2009.

63 A. Cacchioli, F. Ravanetti, R. Alinovi, S. Pinelli, F. Rossi, M. Negri, E. Bedogni, M. Campanini, M. Galetti, M. Goldoni, P. Lagonegro, R. Alfieri, F. Bigi and G. Salviati, *Nano Letters*, 2014, **14**, 4368–4375.

64 Y. Goldberg, M. E. Levinshtein and S. L. Rumyantsev, *Properties of Advanced Semiconductor Materials GaN, AlN, SiC, BN, SiC, SiGe*, John Wiley Sons, New York, 2001.

65 K. Chenoweth, A. C. T. van Duin and W. A. Goddard, *The Journal of Physical Chemistry A*, 2008, **112**, 1040–1053.

66 A. D. Kulkarni, D. G. Truhlar, S. Goverapet Srinivasan, A. C. T. van Duin, P. Norman and T. E. Schwartzentruber, *The Journal of Physical Chemistry C*, 2013, **117**, 258–269.

67 S. Plimpton, *Journal of Computational Physics*, 1995, **117**, 1–19.

68 C. Gougoussis, M. Calandra, A. P. Seitsonen and F. Mauri, *Phys. Rev. B*, 2009, **80**, 075102.

69 P. Giannozzi, S. Baroni, N. Bonini, M. Calandra, R. Car, C. Cavazzoni, D. Ceresoli, G. L. Chiarotti, M. Cococcioni, I. Dabo, A. D. Corso, S. de Gironcoli, S. Fabris, G. Fratesi, R. Gebauer, U. Gerstmann, C. Gougoussis, A. Kokalj, M. Lazzeri, L. Martin-Samos, N. Marzari, F. Mauri, R. Mazzarello, S. Paolini, A. Pasquarello, L. Paulatto, C. Sbraccia, S. Scandolo, G. Sclauzero, A. P. Seitsonen, A. Smogunov, P. Umari and R. M. Wentzcovitch, *Journal of Physics: Condensed Matter*, 2009, **21**, 395502.

70 2017, http://www.quantum-espresso.org.

71 P. E. Blöchl, *Phys. Rev. B*, 1994, **50**, 17953–17979.

72 Y. K. Chang, H. H. Hsieh, W. F. Pong, M.-H. Tsai, K. H. Lee, T. E. Dann, F. Z. Chien, P. K. Tseng, K. L. Tsang, W. K. Su, L. C. Chen, S. L. Wei, K. H. Chen, D. M. Bhusari and Y. F. Chen, *Physical Review B*, 1998, **58**, 9018–9024.

73 F. Neri, F. Barreca, E. Fazio, E. Barletta, G. Mondio, S. Trusso, B. Brendebach and H. Modrow, *J. Vac. Sci. Technol. A*, 2007, **25**, 117–125.

74 M. Liu, X. Yang, Y. Gao, R. Liu, H. Huang, X. Zhou and T. K. Sham, *Journal of the European Ceramic Society*, 2017, **37**, 1253–1259.

75 H. Zhang, Y. Xu, J. Zhou, J. Jiao, Y. Chen, H. Wang, C. Liu, Z. Jiang and Z. Wang, *J. Mater. Chem. C*, 2015, **3**, 4416–4423.

76 L. Liu and T.-K. Sham, *Small*, 2012.

77 Y. Wu, H. Fu, A. Roy, P. Song, Y. Lin, O. Kizilkaya and J. Xu, *RSC Advances*, 2017, **7**, 41812–41818.

78 G. S. Henderson, D. R. Neuville and L. Cormier, *Chemical Geology*, 2009, **259**, 54–62.

79 K. Kim, P. Zhu, N. Li, X. Ma and Y. Chen, *Carbon*, 2011, **49**, 1745 – 1751.

80 M. Pedio, A. Giglia, N. Mahne, S. Nannarone, S. Giovannini, C. Cepek, F. Boscherini, R. Carboni, M. Benfatto and S. Della Longa, *Physica Scripta*, 2005, **T115**, 308–311.

81 M. Tallarida, D. Schmeisser, F. Zheng and F. J. Himpsel, *Surface Science*, 2006, **600**, 3879–3883.

82 G. Monaco, M. Suman, D. Garoli, M. G. Pelizzo and P. Nicolosi, *Journal of Electron Spectroscopy and Related Phenomena*, 2011, **184**, 240–244.

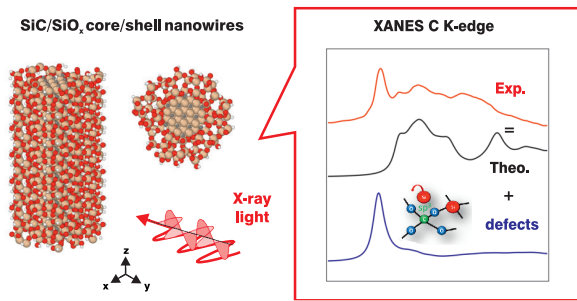83 Jülich Supercomputing Centre, *Journal of large-scale research facilities*, 2015, **1**, year.

Table of Content

A realistic model of SiC/SiO$_x$ core/shell nanowires including several substitutional defects was developed that reproduces experimental X-ray absorption spectra for applications in novel microelectronics devices, cancer therapy and diagnosis.